JOURNAL OF SPACECRAFT AND ROCKETS
Vol. 53, No. 3, May-June 2016



# Speckle Interferometry Tracking of On-Orbit Servicing in Geostationary Orbit

Robert L. Scott*
*Defence Research and Development Canada, Ottawa, Ontario K1A 0Z4, Canada*
and
Alex A. Ellery†
*Carleton University, Ottawa, Ontario, Canada*

DOI: 10.2514/1.A33406

**On-orbit servicing missions in geostationary orbit with intersatellite separations less than 1 km pose a problem for ground-based electro-optical space surveillance sensors. The close separations between the objects subtend angles comparable to the size of turbulence (seeing) cells of Earth's atmosphere. Speckle interferometry using a cross-spectrum approach was explored as a means to overcome atmospheric turbulence to enable measurement of relative positions of on-orbit servicing satellites without the use of adaptive optics and to enable unambiguous positioning of the secondary satellite. A test of this approach using collocated geostationary satellites, acting as on-orbit servicing proxies, found that cross-spectrum measurements can obtain in-track and cross-track relative position precisions better than 100 m when the satellites' apparent angular separations were less than 5 arcseconds. Simulations indicate that the radial position estimates requires 3 h of observation data in order to converge and points to a need for longer observation periods to estimate relative orbits. Brightness differences between the objects did not pose a significant observational limitation as brightnesses of $m_{\text{primary}} = 10.2$, $\Delta m = 0.3$ and $m_{\text{primary}} = 9.1$, $\Delta m = 1.5$ were speckled successfully with relative position estimates obtained.**



## Nomenclature

| | | |
|---|---|---|
| $A$ | = | cross-sectional area, $m^2$ |
| $\boldsymbol{A}$ | = | state dynamics matrix |
| AC | = | autocorrelation |
| $a_p$ | = | pixel pitch, arcseconds/pixel |
| $\boldsymbol{a}_{\text{SRP}}$ | = | solar radiation pressure acceleration, $m/s^2$ |
| CC | = | cross-correlation |
| $C_r$ | = | coefficient of reflectivity |
| $D$ | = | telescope diameter, m |
| $d$ | = | distance between objects, arcseconds |
| $F_S$ | = | fringe separation, cycles/frame |
| $\boldsymbol{f}$ | = | = disturbance matrix, $m/s^2$ |
| $f_l$ | = | focal length, m |
| $f_1$ | = | primary flux, $W/m^2$ |
| $f_2$ | = | secondary flux, $W/m^2$ |
| $h$ | = | altitude, km |
| $\boldsymbol{H}$ | = | observation matrix |
| $\hat{I}(x)$ | = | zero mean image |
| $K_0(\rho)$ | = | Fourier transform of cross-correlation |
| $\hat{K}_0(u)$ | = | Fourier transform of cross-spectrum |
| $M$ | = | satellite mass, kg |
| $m_1$ | = | brightness $i'$ of primary, magnitudes |
| $m_2$ | = | brightness $i'$ of secondary, magnitudes |
| $N$ | = | pixel dimension, pixels |
| $O(\boldsymbol{u})$ | = | object function |
| $\boldsymbol{P}$ | = | solar radiation pressure influence coefficients |
| $\boldsymbol{r}_{\text{Hill}}$ | = | Hill position vector, km |
| $r_0$ | = | Fried parameter, cm |
| $\boldsymbol{r}_1$ | = | inertial position vector of primary, km |
| $\boldsymbol{r}_2$ | = | inertial position vector of secondary, km |
| $\boldsymbol{v}_{\text{Hill}}$ | = | Hill velocity vector, km/s |
| $s$ | = | sidereal angle, deg |
| $\hat{S}(x)$ | = | zero mean specklegram |
| $T_{\text{exp}}$ | = | exposure time, s |
| $t$ | = | time, s |
| $u$ | = | spatial frequency, cycles/frame |
| $[\boldsymbol{x} \quad \boldsymbol{y} \quad \boldsymbol{z}]$ | = | Hill position vector, km |
| $z$ | = | zenith angle, deg |
| $\alpha$ | = | right ascension, declination, deg |
| $\alpha_b$ | = | brightness ratio |
| $\alpha_t$ | = | topocentric right ascension, deg |
| $\boldsymbol{\gamma}_{\text{SRP}}$ | = | differential SRP coefficient, $m^2/kg$ |
| $\delta$ | = | declination, deg |
| $\delta_t$ | = | topocentric declination, deg |
| $\Delta m$ | = | magnitude difference $(m_2 - m_1)$, magnitudes |
| $\Delta \boldsymbol{r}$ | = | inertial relative position vector, km |
| $\Delta\alpha_t$ | = | differential topocentric right ascension, deg |
| $\Delta\delta_t$ | = | differential topocentric declination, deg |
| $\Delta\theta$ | = | isoplanatic angle, arcseconds |
| $\varepsilon$ | = | seeing (full width half maximum) |
| $\epsilon$ | = | measurement noise, rad |
| $\theta$ | = | orientation angle, deg |
| $\lambda$ | = | observation wavelength, nm |
| $\mu_\oplus$ | = | Earth gravitational parameter, $km^3/s^2$ |
| $\zeta$ | = | zenith angle, deg |
| $\rho$ | = | correlation shift or separation distance, arcseconds |
| $\rho_t$ | = | topocentric slant range to primary, km |
| $\boldsymbol{\rho}_1$ | = | primary slant range position vector, km |
| $\boldsymbol{\rho}_2$ | = | secondary slant range position vector, km |
| $\boldsymbol{\Phi}(\boldsymbol{t}, \boldsymbol{t}_0)$ | = | state transition matrix |
| $\omega$ | = | mean motion of geostationary satellite, rad/s |
| $\boldsymbol{\omega}_\times$ | = | skew symmetric matrix |

Received 4 August 2015; revision received 29 November 2015; accepted for publication 30 January 2016; published online 28 April 2016. 

*Defence Scientist, Space Systems and Operations Group, 3701 Carling Avenue.

†Professor, Department of Mechanical and Aerospace Engineering, 1125 Colonel By Drive.

## I. Introduction

THERE are more than 400 active geostationary satellites‡ in geosynchronous equatorial orbit (GEO) providing communi-

‡Data available online at http://www.unoosa.org/pdf/pres/stsc2012/tech-48E.pdf [accessed 11 March 2015].

cations, weather, navigation, early warning, and other services to private, commercial, and government users. The service lifetime of these satellites is fated by finite fuel capacity, battery charge/discharge cycles, and system redundancies, limiting most modern geostationary satellites to approximately 15 years of service life. During launch and early operations, a deployment failure of a solar array or antenna reflector can have large consequences on the services provided by these satellites. Operators have little to no recourse as repairs are currently impossible in GEO orbit.

A technology change is occurring in which autonomous, robotic on-orbit servicing (OOS) systems are showing technical viability. OOS systems could provide fly-around inspection, refueling, repair, antenna or solar array deployment assistance, or deorbit capabilities for orbiting satellites. OOS has historically been performed by astronauts (e.g., [1,2]); however, autonomous robotic OOS has shown continued technological maturity in the past decade, in which several demonstration missions[§] [3,4] were performed. Key OOS robotic operations benchmarks were achieved with the 2007 Orbital Express mission [5] including autonomous proximity operations, satellite captivation, intersatellite refueling, and battery replacement, all with a view toward demonstrating the technologies needed to service satellites in GEO orbit.

These exciting new mission possibilities for geostationary satellite operators will stimulate new considerations for the space surveillance community, which is tasked to track and monitor a new class of formation flight and proximity operations.

## II. OOS Space Surveillance Problem

Space surveillance of GEO is normally performed with optical telescopes. Orbiting objects are imaged and tagged with their positional information relative to the background stars (see Fig. 1). In recent years, the study of closely spaced objects (satellites) in GEO orbit has focused on the proper tagging (identification and association) of clustered geostationary satellites (separations of ∼0.1 deg or ∼74 km, which is the size of neighboring geostationary station-keeping boxes). Another closer proximity case is collocated geostationary satellites, in which two satellites occupy the same geostationary box and tend to have separations of tens of kilometers or less (0.01–0.1 deg of separation when viewed from the ground). In both of these cases, position prediction using general perturbation two-line orbital elements lacks the accuracy needed for simple association between measured and predicted positions of the satellites. While reliably associating satellite identity is a problem for these closely spaced geostationary objects, both of these observation cases are routinely detectable and trackable by ground-based telescopes as separate objects resolved on a charged couple device (CCD) or other detector.

A future OOS mission in GEO poses a new extreme case of close-proximity flight. During OOS, the satellites' separation can be less than 1 km, subtending an angle less than 0.001 deg when viewed from the ground. A 200–1000 m separation distance, when viewed at geostationary ranges (see Fig. 2), is comparable to the angular size of Earth's atmospheric turbulence cells (1–5 arcseconds, ∼5–25 $\mu$rad). Optical detection and tracking of these very closely spaced objects requires a new approach to the imaging and measurement of their positions. An example of geostationary satellites with a close separation similar to the cluster problem is shown in Fig. 1, left. Satellites performing OOS would be much closer together, where the atmospheric point spread function (PSF, the width of the satellite dots in Fig. 1) would merge together (an extreme case of Fig. 1, right), rendering typical object detection techniques (such as pixel clustering) ineffective at measuring the positions of the satellites.

In this work, speckle interferometry using the cross-spectrum, a variant of Labeyrie speckle interferometry [6], was examined to overcome the atmospheric turbulence problem and enable detection and measurement of very closely spaced OOS objects performing uncaptivated proximity operations in GEO. In contrast to prior studies using speckle techniques for space object imaging [7,8], this adaptation concentrates on the detection and tracking of two closely spaced objects in GEO as corrupted by turbulence. Relative position measurements can help assure the safety of flight of OOS proximity operations or determine the relative motion of an unexpected (or unwanted) object in very close proximity to one's satellite for which space security could be of concern. Relative orbit information could help determine object intent as the motion of inert space debris would differ compared to an object performing persistent fly-around or station-keeping maneuvers about a client satellite.

This paper introduces speckle interferometry and the cross-spectrum as adapted for space surveillance for closely spaced objects in Sec. III. An observational model based on telescope viewing geometry while adapting speckle interferometry techniques for GEO monitoring is developed in Sec. IV. A relative motion model based on solar radiation pressure adjusted Clohessy–Wiltshire (Hill) equations of motion is developed in Sec. V, followed by instrument configuration (Sec. VI). As OOS missions are not currently available for observation in geostationary orbit, testing of this approach using a medium aperture telescope was achieved by observing rare, collocated geostationary satellite alignments acting as observational proxies for OOS. The observational results are provided in Sec. VII, and properties of the relative orbit estimates based on the differential angles approach are provided in Secs. IX and X.

Throughout this paper, the naming convention for the client and servicing satellite is as follows: the client satellite (also known as the primary) and the servicer (also known as the secondary) adhere to the following brightness convention. The primary satellite is defined as the brighter of the two objects as it is anticipated that the servicing satellite is likely to be smaller[¶] and therefore less reflective and fainter than a large geostationary communications satellite (the client). The brightness ratio $\alpha_b$ parameterizes the ratio of flux of the secondary

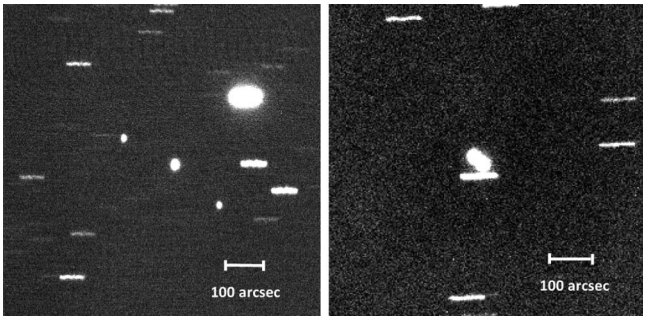


**Fig. 1 (Left) Collocated geostationary satellites. (Right) Optical conjunction of two satellites.**

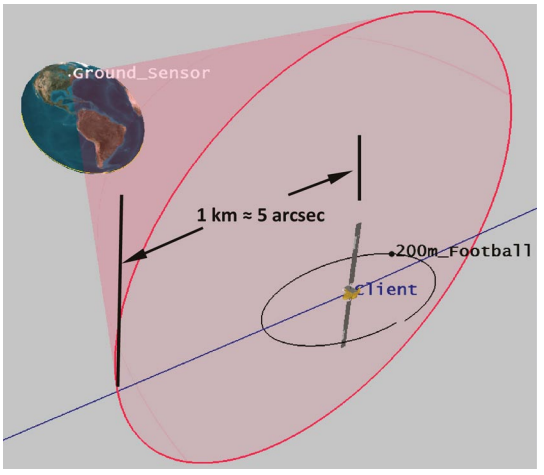


**Fig. 2 Scale sizes of interest for GEO OOS proximity flight.**

[§]Data available online at http://robotics.jaxa.jp/project/ets7-HP/ets7_e/rvd/rvd_index_e.html#FP-1 [retrieved June 2009].

[¶]In instances in which the servicer is brighter than the client, the relative positon vector derived from the following analysis simply needs to be reversed.

object $f_2$ to the primary object $f_1$. Using the respective object magnitudes such that $\Delta m = m_2 - m_1$, $\alpha_b$ is expressed as

$$\alpha_b = \frac{f_2}{f_1} = 10^{-0.4(m_2 - m_1)} \tag{1}$$

## III. Atmospheric Turbulence, Speckle Interferometry, and Imaging

Earth's atmosphere is stratified by layers of varying wind speed, pressure, temperature, and humidity, resulting in turbulence cells that randomly refract light from astronomical sources when observed from the ground. The angle that these turbulence cells subtend is contrasted against the resolving power of a telescope, which can be estimated by the Airy radius ($1.22\lambda/D$), where $\lambda$ is the wavelength and $D$ is the aperture diameter. If the turbulence cells are larger than a telescope's diffraction limit, then short-exposure (~1–20 ms) astronomical images result in speckle patterns that consist of phase-shifted duplications of the object (see Fig. 3, left).

The size of the turbulence cells is characterized by the coherence length $r_0$, known as the Fried parameter [9]. The Fried parameter is used to estimate the size of the turbulence degraded seeing disk (or "seeing"),

$$\varepsilon_{\text{seeing}} \approx \frac{\lambda}{r_0} \tag{2}$$

where $\varepsilon_{\text{seeing}}$ is in radians. Under typical observation conditions, the Fried parameter $r_0$ has a characteristic size of ~10 cm in the visible band, and $r_0$ scales proportionally to $\lambda^{6/5}$. The number of speckles formed within a telescope aperture diameter $D$ is proportional to $(D/r_0)^2$ and is shown in Fig. 4, exhibiting the speckle size $\lambda/D$ and seeing disk $\lambda/r_0$.

The speckle pattern for short exposures will be duplicative over an angular area referred to as the isoplanatic angle. If two astronomical objects are observed with separations larger than this angle, the speckles decorrelate, making interference fringes (Fig. 3, center) less salient. The natural atmospheric aperture that the isoplanatic angle $\Delta\theta$ subtends is estimated [10],

$$\Delta\theta \approx 0.314\frac{r_0}{H} \tag{3}$$

where $H$ is the altitude where most of the seeing distortion occurs (~5 km). Equation (3) shows that the isoplanatic angle increases if $r_0$ increases (seeing becomes steadier). The typical isoplanatic angle varies from 3 to 4 arcseconds [11] and increases with improving seeing conditions.

In this work, acquisition of ground-based speckle measurements of satellites performing OOS in GEO are constrained to the angular size of the isoplanatic patch. Experimental work presented later in this paper found that an upper limit of 5 arcseconds (approximately 1 km separation at GEO ranges) worked well as a natural demarcation for closely spaced satellite objects meeting the upper limit of the atmospheric turbulence aperture. Separations of objects in GEO larger than 5 arcseconds are less likely to benefit from the use of speckle imaging and would be more likely to have higher relative orbit drift rates with respect to one another. In such cases, conventional ground-based detection approaches would be more likely to detect and track these well-separated objects.

Labeyrie [6] published an innovative means to achieve diffraction limited observations of binary stars by stacking and averaging the modulus of the Fourier transforms of multiple short-exposure images. Measurements of the orientation angle and separation of the speckle interference fringes in the frequency plane can directly measure the separation and orientation angle of astronomical objects (Fig. 3, center). A complimentary method, autocorrelation, can be used to produce a quasi image of a binary star pair, albeit with an ambiguity object generated during the transform (Fig. 3, right). Both techniques result in a 180 deg ambiguous position of the secondary object due to the functional symmetry of the Fourier transform and the autocorrelation. This is problematic for automated space surveillance orbit determination systems that rely on unambiguous positioning of objects in order to reliably estimate their trajectories. A direct approach to eliminate the ambiguity called directed vector autocorrelation [12] can be implemented; however, significant computational overhead is imposed for relatively modest detector arrays. Larger pixel arrays are preferred for space surveillance to ease the centering and tracking of Earth orbiting objects with narrow field-of-view telescopes.

An alternative method to resolve the direction ambiguity, while simultaneously alleviating computational expense, is to invoke the cross-spectrum of the square of a zero-mean speckle image. This approach found application in the binary star astronomy community and was described by Aristidi et al. [13]. This technique's repeated

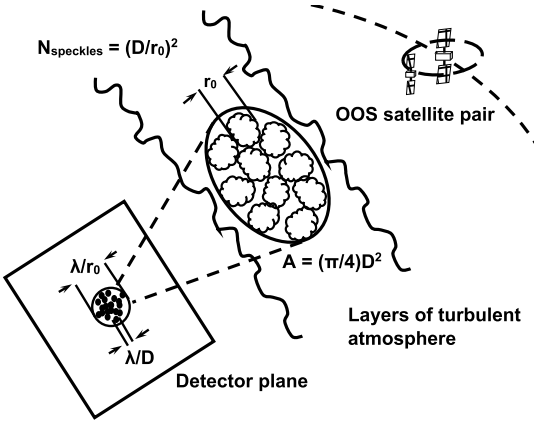


**Fig. 4 Turbulence cells of size $r_0$ forming speckles on a detector.**

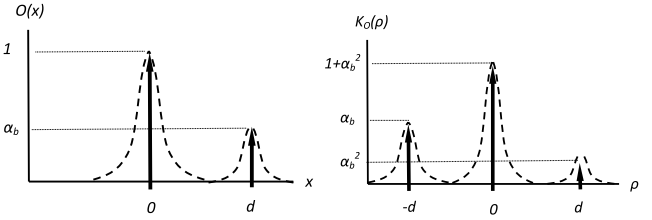


**Fig. 5 (Left) Object function $O(x)$. (Right) Cross-correlation of the object.**

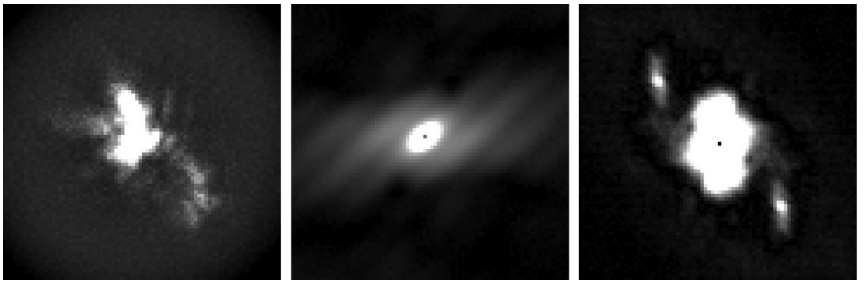

**Fig. 3 (Left) Speckle image of binary star. (Center) Power spectrum fringes. (Right) Autocorrelation.**

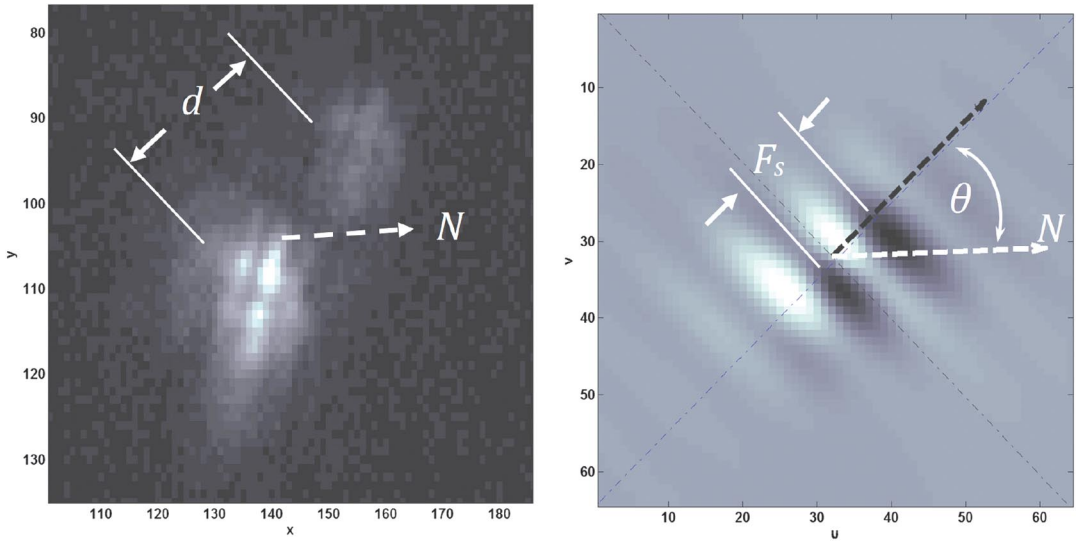


**Fig. 6 (Left) Specklegram of binary star STF 738AB. (Right) Imaginary component of its cross-spectrum.**



use of the fast Fourier transform greatly lessens the impact of pixel array size on computational time. In addition, the extraction of the cross-spectrum's complex component permits direct, unambiguous direction finding to the secondary.

The cross-spectrum is formed by taking the Fourier transform of the cross-correlation of an image,

$$K_0(\rho) = \int_{-\infty}^{\infty} O^2(x) O(x+\rho)\,\mathrm{d}x \tag{4}$$

where $O(x)$ is defined as

$$O(x) = \delta(x) + \alpha_b \delta(x-d) \tag{5}$$

where $\rho$ is the positional shift during cross-correlation, $d$ is the separation between the objects, $\alpha_b$ is the brightness ratio defined in Eq. (1), and the object positions are modelled as Dirac delta functions $\delta(\rho - x)$. A graphical representation of $O(x)$ and $K_0(\rho)$ is shown in Fig. 5.

Expanding the integral in Eq. (4) creates a three-pulse cross-correlation:

$$K_0(\rho) = (1+\alpha_b^3)\delta(\rho) + \alpha_b^2 \delta(\rho - d) + \alpha_b \delta(\rho + d) \tag{6}$$

The cross-correlation produces a quasi image in which the central peak represents the primary object surrounded by two companions, each with a separation $d$. Although the true position of the secondary is inferable as the smaller peak of the cross-correlation, directly detecting it is not viable as the secondary (and quite possibly the tertiary) peak may be too small for image processing techniques to reliably detect.

To determine the unambiguous direction and distance to the secondary object, the cross-spectrum of $K_0(\rho)$ is formed by taking its Fourier transform and isolating its real and imaginary components:

$$Re\{K_0(u)\} = (1+\alpha_b^3) + \alpha_b(1+\alpha_b)\cos(2\pi u d) \tag{7}$$

$$Im\{K_o(u)\} = \alpha_b(1-\alpha_b)\sin(2\pi u d) \tag{8}$$

The period between the imaginary fringes in Eq. (8) is periodic in $1/d$ to the objects' true spatial separation.

Aristidi et al. [13] identified that the slope of the imaginary component at the center of its fringe profile directly identifies the direction toward the secondary:

$$\text{slope} = \left\{\frac{\mathrm{d}}{\mathrm{d}u} Im[\hat{K}_o(u)]\right\}_{u=0} = 2\pi d \alpha_b (1-\alpha_b) \tag{9}$$

This property of the cross-spectrum uniquely identifies the direction to the secondary object (see Fig. 6, right) as the fringe gradient is positive in the direction to the more faint object.** The orientation angle $\theta$ can be found by taking the angle perpendicular to the fringes. Applying knowledge of the fringe gradient from Eq. (9), the vector to the secondary object is directly found. All the information required to describe the relative position ($d$, $\theta$) between the two objects is contained within the imaginary component of the cross-spectrum.

For practical image processing using the cross-spectrum, zero mean images $\hat{I}(x)$ and of the speckles $\hat{S}(x)$ must be formed in order to ignore cross-correlation bias terms that appear during the image processing of real speckles [13],

$$\hat{S}(x) = S(x) - \bar{S} \tag{10}$$

and

$$\hat{I}(x) = I(x) - \bar{I} \tag{11}$$

where the overbar denotes the mean value. This permits the approximations for cross-spectrum image processing,

$$K_{\hat{I}}(\rho) = K_{\hat{S}}(\rho) * K_O(\rho) \tag{12}$$

and

$$\hat{K}_{\hat{S}}(u) = \hat{K}_{\hat{S}}(u) \cdot \hat{K}_O(u) \tag{13}$$

where the cross-spectrum of the zero mean image $\hat{I}$ is computed by taking the ensemble average of

$$\hat{K}_{\hat{I}}(u) = \langle \mathcal{F}(\hat{I}^2) \cdot \mathcal{F}(\hat{I})^* \rangle \tag{14}$$

and $*$ is the complex conjugate.

Assuming a symmetric shape of the speckle $\hat{K}_{\hat{S}}(u)$ in the frequency domain, the signal equation for the imaginary component of the cross-spectrum becomes

$$Im[\hat{K}_{\hat{I}}(u)] = \hat{K}_{\hat{S}}(u)[\alpha_b(1-\alpha_b)\sin(2\pi u d)] \tag{15}$$

The separation distance between the two objects in the frequency domain is simply $d = 1/F_s$, where $F_s$ is the fringe separation in cycles

**The brightness ratio is defined to be $0 < \alpha_b <= 1$.

per frame. $F_s$ is reckoned by measuring the spatial frequency (distance) between the first dark minima [14] of the cross-spectrum (see Fig. 6, right). For frames of $N$ pixels per frame with a pixel pitch of $a_p$ (arcsecond/pixel), the measured distance $d$ between the objects is

$$d = Na_p/F_s \tag{16}$$

## IV. Observational Model and Reference Frames

Measurements of satellites performing OOS using speckle imaging observations $(\rho, \theta)$ are differential angles describing the relative angular position of the servicer with respect to the client. For these measurements to be useful for relative orbit determination, they must be transformed to a radial, in-track, cross-track frame (such as the Hill frame [15]; see Fig. 7). This approach is in contrast to typical angles-only ground-based observations of satellites, which measure satellite positions with respect to Earth's geocenter by collecting satellite angular positions relative to background stars.

The position of the servicing satellite relative to the client is expressed as the difference between the slant range vectors $\boldsymbol{\rho}$ and the absolute positional vectors of the satellites $\boldsymbol{r}$. The vectors adhere to the conventions identified in [15],

$$\Delta\boldsymbol{r} = \boldsymbol{r}_2 - \boldsymbol{r}_1 = \boldsymbol{\rho}_2 - \boldsymbol{\rho}_1 \tag{17}$$

where $\Delta\boldsymbol{r}$ is the position of the servicer with respect to the client.

### A. Observer's Topocentric Reference Convention and Measurements

Differential angle measurements collected by a speckle imaging system are referenced to the true equator and equinox of date, or true of date (TOD) frame [16]. This coordinate frame is a good match to GEO object motion and the fixed polar alignment of an equatorially mounted telescope and also eases the calibration of the orientation angle with respect to celestial north using the star trails drift method [15].

In this TOD frame, geocentric right ascension ($\alpha$) and declination ($\delta$) coordinates describe the angular position of a geostationary satellite on the celestial sphere. A ground-based observer measures the satellite's position shifted by parallax resulting in topocentric right ascension ($\alpha_t$) and declination ($\delta_t$) measurements which differ from the satellite's geocentric coordinates. This difference is modeled by using components of the slant range vector from the satellite to the observer. The topocentric angular measurements are thus defined as

$$\tan(\alpha_t) = \frac{\rho_y}{\rho_x} \tag{18}$$

and

$$\sin(\delta_t) = \frac{\rho_z}{\|\boldsymbol{\rho}\|} \tag{19}$$

An observation vector $\boldsymbol{y}_i$ is formed by transforming the speckle measurements $(d, \theta)$ into time and differential right ascension and declination measurements ($t$, $\Delta\alpha_t$, and $\Delta\delta_t$, respectively) using Eq. (20). Right ascension measurements require division by the object's topocentric declination to correctly scale the celestial longitude,

$$\boldsymbol{y}_i = \begin{bmatrix} \Delta\alpha_t \\ \Delta\delta_t \end{bmatrix}_i = \begin{bmatrix} \frac{d\,\sin(\theta)}{\cos(\delta_t)} \\ d\,\cos(\theta) \end{bmatrix}_i \tag{20}$$

### B. Transformation of Observations from Hill Frame to Differential Angles

A transformation relating differential angles to the Hill (rotating) state coordinates is required. This is achieved by using a series of transformations and is described in [15]. Taking the differentials of Eqs. (18) and (19) yields

$$\begin{bmatrix} \Delta\alpha_t \\ \Delta\delta_t \end{bmatrix} = \frac{1}{\|\boldsymbol{\rho}^2\|} \begin{bmatrix} -\rho_y & \rho_x & 0 \\ \frac{-\rho_x\rho_z}{(\rho_x^2+\rho_y^2)} & \frac{-\rho_y\rho_z}{(\rho_x^2+\rho_y^2)} & 1 \end{bmatrix} \begin{bmatrix} d\rho_x \\ d\rho_y \\ d\rho_z \end{bmatrix} \tag{21}$$

$$\Delta\boldsymbol{r} = [\, d\rho_x \quad d\rho_y \quad d\rho_z \,]^T \tag{22}$$

$\Delta\boldsymbol{r}$ is referenced to the TOD frame. This position vector needs to be rotated to Hill coordinates using the radial-transverse-normal (RSW) [16] frame by forming the rotation matrices for an inertial position vector

$$[\mathbf{R} \mid \mathbf{S} \mid \mathbf{W}] = \mathbf{R}_2(-\delta)\mathbf{R}_3(\alpha) \tag{23}$$

where $\alpha$ and $\delta$ are the geocentric right ascension and declination of the primary satellite and $\boldsymbol{R}_2$ and $\boldsymbol{R}_3$ are the rotation matrices about their corresponding axes. The differential position vector expressed in the TOD frame is found by inverting the [$\boldsymbol{RSW}$] transformation matrix and multiplying

$$\begin{bmatrix} \Delta\vec{\mathbf{r}}_{TOD} \\ \Delta\vec{\mathbf{v}}_{TOD} \end{bmatrix} = [\mathbf{R} \mid \mathbf{S} \mid \mathbf{W}]^{-1} \begin{bmatrix} \Delta\vec{\mathbf{r}}_{RSW} \\ \Delta\vec{\mathbf{v}}_{RSW} \end{bmatrix} \tag{24}$$

where $\boldsymbol{\Delta r}_{\mathrm{TOD}}$ and $\boldsymbol{\Delta v}_{\mathrm{TOD}}$ are the differential position and velocity of the secondary with respect to the client. The differential position vector in the RSW frame is identical to the Hill position vector, provided the distance between the objects is very small, permitting subtle frame corrections [17] to be ignored.

Equation (24) is expanded by accounting for the rotating nature of the RSW frame as

$$\begin{bmatrix} \Delta\vec{\mathbf{r}}_{TOD} \\ \Delta\vec{\mathbf{v}}_{TOD} \end{bmatrix} = [\mathbf{R} \mid \mathbf{S} \mid \mathbf{W}]^{-1} \left[\begin{array}{c|c} \mathbf{I}_{3\mathrm{x}3} & \mathbf{0}_{3\,x\,3} \\ \hline [\boldsymbol{\omega}_{\times}] & \mathbf{I}_{3\mathrm{x}3} \end{array}\right] \begin{bmatrix} \vec{\mathbf{r}}_{\mathbf{Hill}} \\ \vec{\mathbf{v}}_{\mathbf{Hill}} \end{bmatrix} \tag{25}$$

where $\boldsymbol{I}$ is a $3 \times 3$ identity matrix and the skew symmetric matrix $\boldsymbol{\omega}_{\times}$ corrects the Hill velocity due to the rotating nature of the Hill frame [16]. After combining Eqs. (23) and (25), the relationship between the state $[\boldsymbol{r}_{\mathrm{Hill}}, \boldsymbol{v}_{\mathrm{Hill}}]^T$ the differential angles measurements, based on Hill coordinates, becomes

$$\begin{bmatrix} \Delta\alpha_t \\ \Delta\delta_t \end{bmatrix} = \frac{1}{\rho_t} \begin{bmatrix} h_1 & h_2 & h_3 & 0 & 0 & 0 \\ h_4 & h_5 & h_6 & 0 & 0 & 0 \end{bmatrix} \begin{bmatrix} \boldsymbol{r}_{\mathrm{Hill}} \\ \boldsymbol{v}_{\mathrm{Hill}} \end{bmatrix} \tag{26}$$

with components consisting of

$$h_1 = \frac{\sin(\alpha - \alpha_t - \delta) + \sin(\alpha - \alpha_t + \delta)}{2\,\cos(\delta_t)} \tag{27}$$

$$h_2 = \frac{\cos(\alpha - \alpha_t)}{\cos(\delta_t)} \tag{28}$$

$$h_3 = \frac{\cos(\alpha)\sin(\alpha_t)\sin(\delta) - \sin(\alpha)\cos(\alpha_t)\sin(\delta)}{\cos(\delta_t)} \tag{29}$$

$$h_4 = \cos(\delta_t)\sin(\delta) - \cos(\alpha)\cos(\alpha_t)\cos(\delta)\sin(\delta_t) - \sin(\alpha)\cos(\delta)\sin(\alpha_t)\sin(\delta_t) \tag{30}$$

$$h_5 = \sin(\alpha - \alpha_t)\sin(\delta_t) \tag{31}$$

$$h_6 = \cos(\delta_t)\cos(\delta) + \cos(\alpha)\cos(\alpha_t)\sin(\delta)\sin(\delta_t) + \sin(\alpha)\sin(\alpha_t)\sin(\delta)\sin(\delta_t) \tag{32}$$

where geocentric ($\alpha$, $\delta$) and topocentric ($\alpha_t$, $\delta_t$) angles are denoted. Note that for midlatitude, ground-based observers Eq. (26) can be simplified using small angle approximations as $\delta_t$ and $(\alpha - \alpha_t)$ cannot exceed 8 deg.

## V. Linearized Relative Motion Model and Solar Radiation Pressure

The linearized Clohessy–Wiltshire [18] or Hill [19] equations are used to model the relative motion of two closely spaced satellites in geostationary orbit [20]. The radial $x$, in-track $y$, and cross-track $z$ motion of the secondary satellite relative to the (client) position is described by the second-order coupled differential equations

$$\begin{bmatrix} \ddot{x} \\ \ddot{y} \\ \ddot{z} \end{bmatrix} = \begin{bmatrix} 2\omega\dot{y} + 3\omega^2 x \\ -2\omega\dot{x} \\ -\omega^2 z \end{bmatrix} + \begin{bmatrix} a_x \\ a_y \\ a_z \end{bmatrix} \tag{33}$$

where $\omega$ is the mean orbital motion of the GEO satellite and $[a_x, a_y, a_z]^T$ are disturbance accelerations. Recasting Eq. (34) into state space form

$$\dot{\boldsymbol{x}} = \boldsymbol{A}\boldsymbol{x} + \boldsymbol{f} \tag{34}$$

the state expressed in the Hill frame is

$$\boldsymbol{x} = [x \quad y \quad z \quad \dot{x} \quad \dot{y} \quad \dot{z}]^T \tag{35}$$

and the dynamics $\boldsymbol{A}$ and disturbance $\boldsymbol{f}$ are [Eqs. (36) and (37)]

$$\boldsymbol{A} = \begin{pmatrix} 0 & 0 & 0 & 1 & 0 & 0 \\ 0 & 0 & 0 & 0 & 1 & 0 \\ 0 & 0 & 0 & 0 & 0 & 1 \\ 3\omega^2 & 0 & 0 & 0 & 2\omega & 0 \\ 0 & 0 & 0 & -2\omega & 0 & 0 \\ 0 & 0 & -\omega^2 & 0 & 0 & 0 \end{pmatrix} \tag{36}$$

$$\boldsymbol{f} = (0 \quad 0 \quad 0 \quad a_x \quad a_y \quad a_z)^T \tag{37}$$

and the state space representation can be written

$$\boldsymbol{x}(t) = \boldsymbol{\Phi}_u(t, t_0)\boldsymbol{x}(t_0) \tag{39}$$

where $(t, t_0)$ are the current time and epoch time, respectively, and $\boldsymbol{\Phi}_u$ is the $6 \times 6$ state transition matrix of interior algebraic expressions in Eq. (38).

Perturbations due to aspheric Earth gravity and third-body accelerations can be ignored as the close proximity of OOS satellites effectively cancels these perturbations' effects [20]. Solar radiation pressure $\boldsymbol{a}_{\text{SRP}}$ does incur a perturbation due the difference between the area-to-mass ratios of the two objects [Eqs. (40–42)],

$$\boldsymbol{a}_{\text{SRP}} = -P_{\text{sun}}\left[\left(\frac{C_R A}{M}\right)_2 - \left(\frac{C_R A}{M}\right)_1\right]\frac{\boldsymbol{r}_{\text{Sun}}}{|\boldsymbol{r}_{\text{Sun}}|^3} \tag{40}$$

or written as

$$\boldsymbol{a}_{\text{SRP}} = -P_{\text{Sun}}\gamma\frac{\boldsymbol{r}_{\text{Sun}}}{|\boldsymbol{r}_{\text{Sun}}|^3} \tag{41}$$

and forming

$$\gamma = \left(\frac{C_R A}{M}\right)_2 - \left(\frac{C_R A}{M}\right)_1 \tag{42}$$

where $\gamma$ is the differential solar radiation pressure coefficient, $C_R$ is the reflectivity coefficient, and $P_{\text{sun}}$ is solar radiation pressure constant ($4.56 \times 10^{-6}$ Nm$^{-2}$).

To incorporate the effects of solar radiation pressure, the approach of [20] is used to integrate the equations of motion and is described in Appendix A. After inclusion of the perturbation accelerations $p_1 \ldots p_6$ [Eqs. (A4–A9)], the state transition matrix is augmented by

$$\boldsymbol{\Phi}(t_1, t_0) = \left(\begin{array}{c:c} \boldsymbol{\Phi}_u & \begin{matrix} p_1(\alpha_1, \alpha_0) \\ \vdots \\ p_6(\alpha_1, \alpha_0) \end{matrix} \\ \hdashline 0.....0 & 1 \end{array}\right) \tag{43}$$

and the state is augmented with the differential solar radiation pressure coefficient $\gamma$,

$$\boldsymbol{x} = [x \quad y \quad z \quad \dot{x} \quad \dot{y} \quad \dot{z} \quad \gamma]^T \tag{44}$$

Estimating $\gamma$ with the relative orbital state parameters provides the difference of the two satellites' area-to-mass ($A/m$) ratios leading to additional insight about the servicing satellite size if either satellite's $A/m$ is known a priori.

With the dynamics model described, the measurement equation is summarized as

$$\boldsymbol{y}_i = \boldsymbol{H}\boldsymbol{x} + \boldsymbol{\varepsilon} \tag{45}$$

and the measurement sensitivity matrix $\boldsymbol{H}$ of Eq. (26) is simplified assuming a GEO satellite with zero inclination,

A closed-form solution [16] for the case of unperturbed motion is ($\boldsymbol{f} = 0$) is given by

$$\begin{bmatrix} x(t) \\ y(t) \\ z(t) \\ \dot{x}(t) \\ \dot{y}(t) \\ \dot{z}(t) \end{bmatrix} = \begin{bmatrix} 4 - 3\cos(\omega_\oplus t) & 0 & 0 & \frac{1}{\omega_\oplus}\sin(\omega_\oplus t) & \frac{2}{\omega_\oplus}[1 - \cos(\omega t)] & 0 \\ 6\omega[\sin(\omega_\oplus t) - \omega_\oplus t] & 1 & 0 & \frac{2}{\omega_\oplus}[\cos(\omega_\oplus t) - 1] & \frac{1}{\omega_\oplus}[4\sin(\omega_\oplus t) - 3\omega_\oplus t] & 0 \\ 0 & 0 & \cos(\omega_\oplus t) & 0 & 0 & \frac{1}{\omega_\oplus}\sin(\omega_\oplus t) \\ 3\omega_\oplus \sin(\omega_\oplus t) & 0 & 0 & \cos(\omega_\oplus t) & 2\sin(\omega_\oplus t) & 0 \\ 6\omega_\oplus[\cos(\omega_\oplus t) - 1] & 0 & 0 & -2\sin(\omega_\oplus t) & 4\cos(\omega_\oplus t) - 3 & 0 \\ 0 & 0 & -\omega_\oplus \sin(\omega_\oplus t) & 0 & 0 & \cos(\omega_\oplus t) \end{bmatrix} \begin{bmatrix} x_0 \\ y_0 \\ z_0 \\ \dot{x}_0 \\ \dot{y}_0 \\ \dot{z}_0 \end{bmatrix} \tag{38}$$

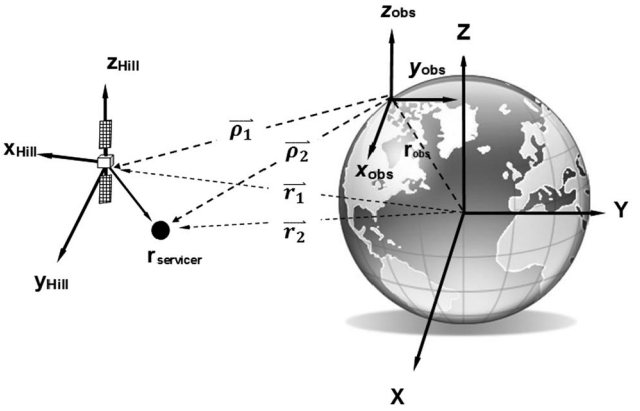


**Fig. 7 Observational geometry [18] for the client, servicer, and ground-based observer.**

$$\boldsymbol{H} = \frac{1}{\rho_t}\begin{bmatrix} \frac{\sin(\alpha-\alpha_t)}{\cos(\delta_t)} & \frac{\cos(\alpha-\alpha_t)}{\cos(\delta_t)} & 0 & 0\ 0\ 0\ 0 \\ -\cos(\alpha-\alpha_t)\sin(\delta_t) & \sin(\alpha-\alpha_t)\sin(\delta_t) & \cos(\delta_t) & 0\ 0\ 0\ 0 \end{bmatrix} \tag{46}$$

and $\varepsilon$ is the measurement noise in differential right ascension and declination. For equatorial GEO satellites, the $\boldsymbol{H}$ matrix is composed of constant terms, which linearizes the observation model by parameterizing the geometry of the satellite pair with the quasi-constant values of $\rho_t$, $(\alpha - \alpha_t,)$, and $\delta_t$.

## VI. Instrument Configuration and Detectors

A speckle interferometer designed to track OOS in GEO requires a harmonization between the competing needs of detectability of the faint satellite target while exposing the imager with exposure times between 10–20 ms in order to freeze atmospheric turbulence. Proper sampling of the telescope's PSF is a key requirement. The size of the telescope's PSF can be estimated as PSF $= \lambda f/D$, where $\lambda$ is the center wavelength of observation and $f$ is the focal length of the telescope. Nyquist sampling is required such that a minimum of 2 pixels traverses the Airy radius in order to properly sample the speckle. Telescopes are often augmented with barlow lenses or microscope objectives to project the PSF across a detector's pixels in order to achieve Nyquist sampling for many telescopes performing speckle interferometry.

Speckle interferometry often employs narrowband filters to ensure that chromatic dispersion [21], the tendency of Earth's atmosphere to refract light similar to that of a prism, is minimized. Reference [21] recommends that the total dispersion should be less than of the speckle size for proper astrometric measurement. Chromatic dispersion is a function of zenith angle $z$ with negligible dispersion occurring at zenith ($z = 0$ deg) and as much as 0.7 arcseconds of chromatic dispersion at $z = 60$ deg for $V$-band wavelengths. Risley prisms can be used to correct this effect, but a less optically complex approach is to use near-infrared filters of 700–900 nm (see Fig. 8). Sloan $i'$ infrared filters lessen the need for dispersion corrective equipment as the error incurred by their use is ~0.4 arcseconds at $z = 60$ deg. In addition, the use of this filter bandpass helps reject lunar stray light, increasing the signal-to-noise ratio for faint satellite speckles during bright lunation. The Sloan $i'$ filter was chosen to simplify the optical train at the back of the telescope and to lessen sky glow from stray light sources.

## VII. Test Observations on Geostationary Satellites

OOS missions are not currently being flown in geostationary orbit, making the testing of the cross-spectrum differential angles approach problematic. Binary stars can be used as testing and calibration proxies; however, they lack observable relative motion characteristic of OOS formation flight. An alternative satellite proxy is possible, but careful planning, good timing, and favorable weather are required. Collocated geostationary satellites are known to occasionally align

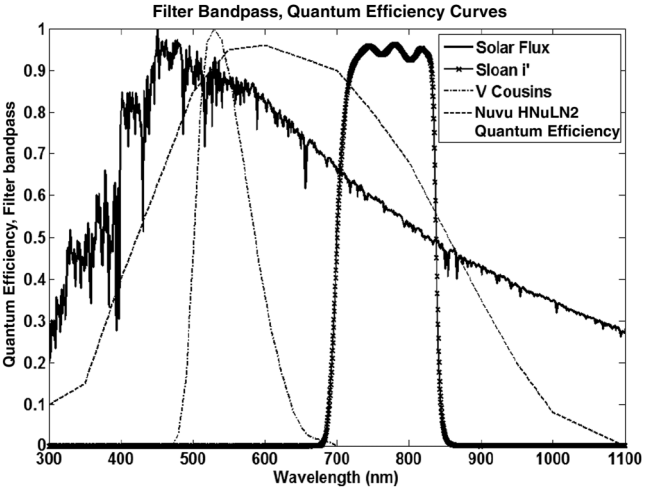


**Fig. 8 Filter band pass of Sloan $i'$ filter and detector quantum efficiency.**

[22] or optically conjunct [15] with respect to a ground observer for ~10–15 min intervals on a monthly to quarterly basis. Occasionally, this alignment occurs at night and with angular separations less than the isoplanatic limit (<5 arcseconds), making these rare events possible test observation candidates. Collocated satellites move in relative motion ellipses considerably larger than what a true OOS mission would perform; however, the experience gained using real satellite speckles would be valuable to test the image processing approach.

Geostationary satellites are known to exhibit diurnal variations in their brightness, forcing the need for a sensitive, large aperture instrument as these alignments (optical conjunctions [15]) could occur when a satellite pair is faint due to poor phase angle illumination. An observation campaign using the 1.6 m telescope at the Mont Mégantic observatory [23] (see Fig. 9) was granted for two weeks in February 2014. Observations of optical conjunctions of collocated geostationary satellites Anik F1, Anik F1R, and Anik G1 meeting the isoplanatic constraint were performed.

A 1024 × 1024 Nuvu EM N2 Nitrogen-cooled, electron multiplied charged couple device (EMCCD) [24] (see Fig. 10) was affixed to the telescope's prime focus along with an 8x arrangement of parfocal barlow lenses achieving 3.3 pixel per PSF sampling of the instrument speckles. The long focal length of this system resulted in a narrow field of view ($27 \times 27$ arcseconds$^2$), forcing the need to acquire and center the collocated satellites using a separate low-light camera. Instrument configuration and calibration details for speckle imaging of satellites are described in [15].

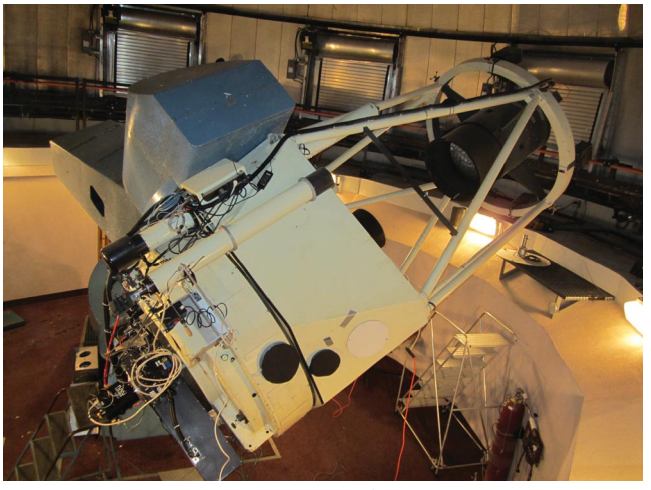

**Fig. 9 The 1.6 m Mont Mégantic telescope.**


**Fig. 10 (Left) EMCCD and barlows. (Right) Fabric covering to reject stray light.**

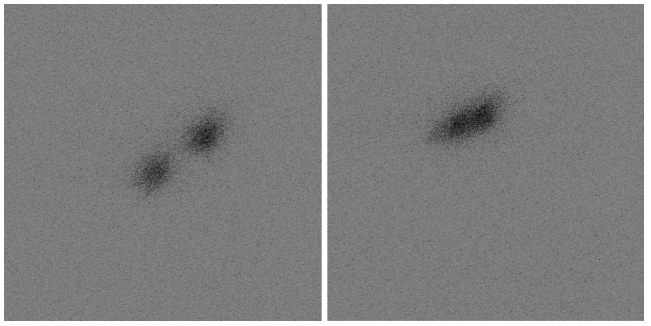

**Fig. 11 (Left) Anik F1R (lower left) and Anik G1. (Right) Both satellites 6 min later.**

Nine days of heavy clouds and high winds prevented observation for the majority of the observation grant. Fortunately, clear weather and two separate optical conjunctions, one between satellite pairs Anik G1 and Anik F1R with a forecasted closest separation of 1.2 arcseconds and a second between Anik G1 and Anik F1 with a separation less than 6 arcseconds, were forecasted for 18 February 2014. The average seeing condition varied between 2.5 to 3.5 arcseconds with occasional periods during which the seeing degraded to greater than 4.5 arcseconds. Despite the clear weather forecast, the surface wind speed of 17 km/h and frequent wind gusts led to marginally acceptable seeing for speckle interferometry. When both satellites were visually estimated to be within 6 arcseconds of one another (see Fig. 11), the EMCCD was set to continuously acquire 10 ms images at a rate of 20 Hz. Image data were stored on the camera control laptop for later processing.

The image processing sequence used the general approach described in [15] but was modified in this analysis by invoking additional processing steps. Autocorrelated imaginary fringes were Sobel filtered to detect linear features, helping to alleviate the Radon transform's locking issue originally discussed in [15]. A correction was also applied to remove the convolution of the telescope and atmospheric PSF on the fringes by fitting a Moffat profile [25] parallel to the fringes to remove the effect of the atmospheric and telescope PSF. This corrects the effect where the fringe minima artificially move inward due to the convolution of the PSF shape onto the fringes [14], distorting the relative astrometric positions of the two objects.

It was found that the cross-spectrum image processing is particularly sensitive to cosmic ray hits on the images (Fig. 12), provoking three-object fringing in the cross-spectrum. Signal from a cosmic ray is comparable to the intensity from both satellites when speckle imaged, and the cross-spectrum invokes another set of fringes, which corrupts the fringe minima detection process. A simple background standard deviation monitor was implemented to remove cosmic ray corrupted frames from the stacking process, and this simple filtering resulted in more reliable detection of fringe minima.

## VIII. Observations of Anik G1 and Anik F1R

The satellite pair Anik G1 (primary) and Anik F1R (secondary) began its optical conjunction, relative to the Mont Mégantic observatory, on 18 February 2015 02:05 UTC. The pair was observed for 10 min before and after the closest apparent approach. The satellites' brightness difference was $\Delta m = 0.36$ magnitudes ($\alpha_b = 0.72$) corresponding to 10.23 and 10.59 magnitudes for the primary and secondary satellites, respectively.

Figure 13 shows selected frames from the data processing of this optical conjunction. Frame time $t$ and $d$, $\theta$ measurements are shown in the first column. Raw frames are shown in second column, and raw cross-spectrum plots of $Im\{K_o(u)\}$ are shown in the third. The autocorrelated (AC) fringes are shown in the fourth column and were used for Sobel edge detection to determine the orientation angle of the fringes. The fifth column shows the Moffat corrected fringe profile with the first minima marked with vertical red lines. The distance between these fringe minima is $F_s$.

Figure 14 shows the measured separation distance and orientation angle of Anik F1R relative to Anik G1. The satellites closed to within 1.2 arcseconds at $t = 131.5$ min UTC. The seeing (bottom left of Fig. 14) was computed using a separate Fourier analysis to estimate the width of the full width half maximum of the atmospheric point spread function. Weakness was observed, however, at $t = 131.5$ and 132.1 min as the orientation angle was not correctly found. This was attributed to the closest separation of the two objects causing a high degree of fringe rotation due to the apparent motion of the objects. During the stacking process, these fringes are rotationally smeared, making the image processor's Sobel filter unable to identify a clear linear fringe structure. When the objects separated by more than 1.5 arcseconds, the linear fringe structure was reformed, and good tracking performance was observed. Also notable from Fig. 14 is the separation ($\rho$) trend departure at the start of the track at $t = 126.5$ min. At these times, the satellite separations exceeded 5

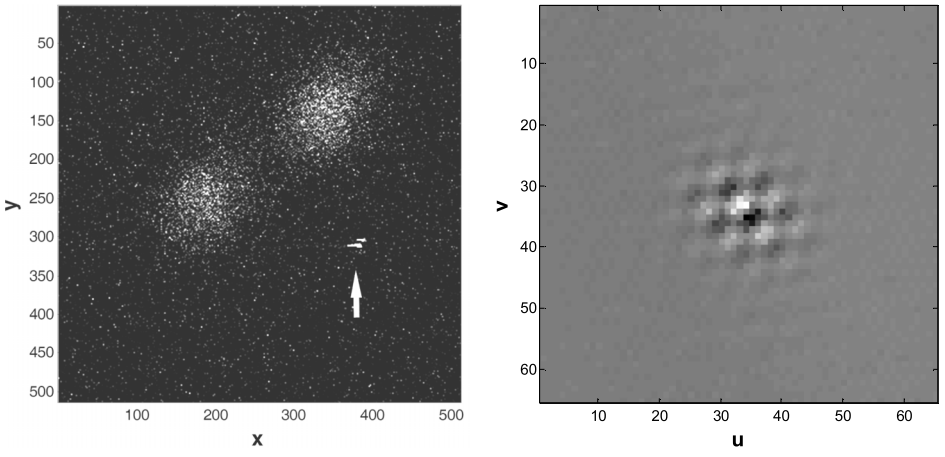


**Fig. 12 (Left) Cosmic ray strike. (Right) Unwanted three-object fringing of the cross-spectrum.**

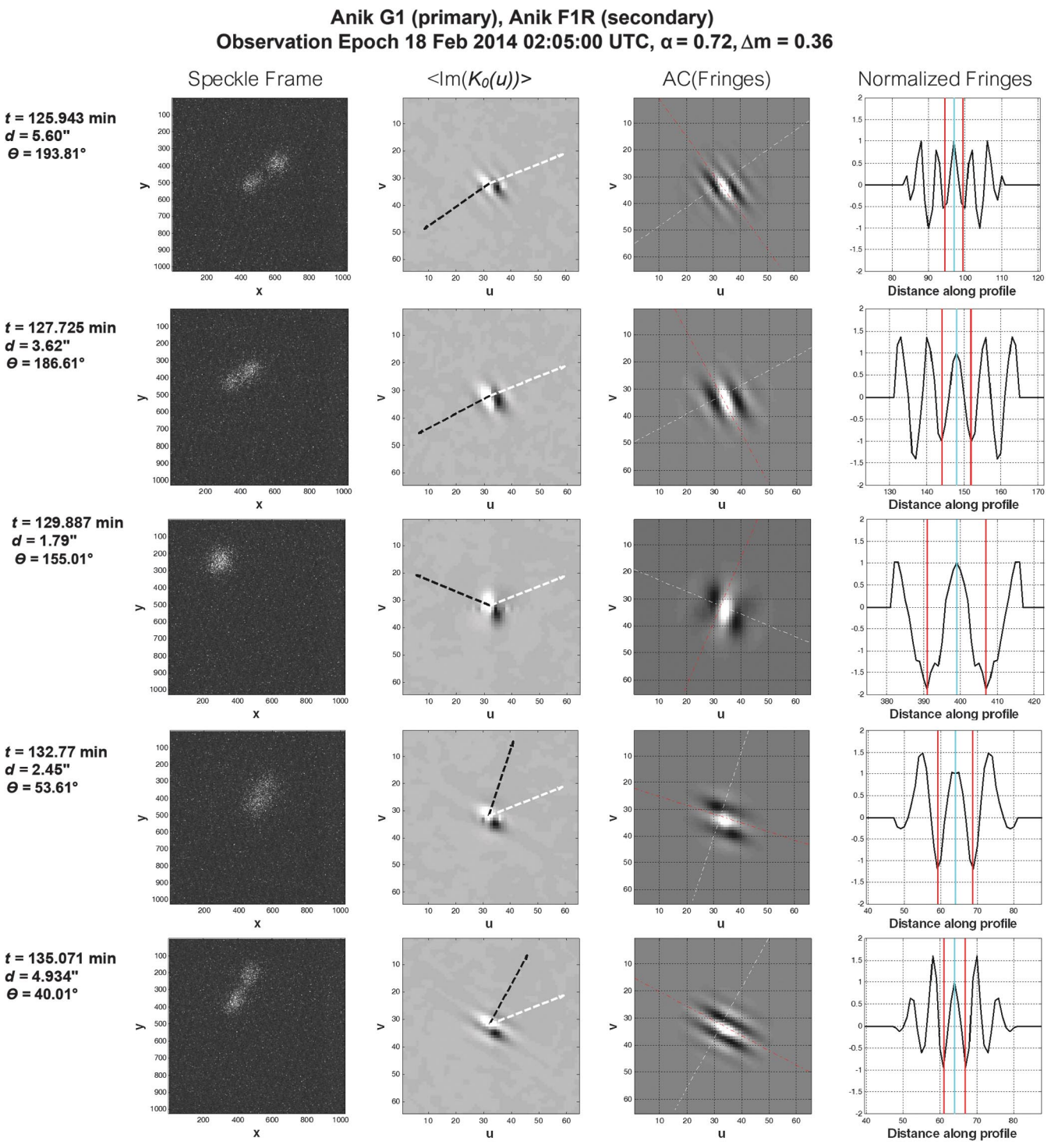


**Fig. 13 Anik G1 and Anik F1R selected frames from data processing. Anik G1 (primary) and Anik F1R (secondary) observation epoch on 18 February 2014, 02:05:00 UTC, $\alpha = 0.72$, $\Delta m = 0.36$.**

arcseconds, which is larger than the isoplanatic angle, suggesting that decorrelation of the speckles caused the erratic separation measurements at these times.

Differential angular measurements ($\Delta\alpha$ and $\Delta\delta$) were computed using the $d$, $\theta$ measurements and were compared to reference differential angles computed using the satellite operator ephemerides (Fig. 15). The track closely adhered to these ephemerides with exceptions at the beginning, closest approach, and end of the track. It was found that the additional image processing steps (Moffat correction and Sobel edge detection of the autocorrelated fringes) markedly improved the $\Delta\alpha$ and $\Delta\delta$ measurement residuals in comparison to previous processing [15] in which biases exceeding 0.5 arcseconds were reported. Current processing measurement noise levels in $\Delta\alpha$ and $\Delta\delta$ were characterized to be 0.18 and 0.25 arcseconds and were subsequently used for relative orbit estimation in the next section.

The second optical conjunction between Anik F1 (primary) and Anik G1 (secondary) began at 18 February 04:43 Universal Coordinated Time (UTC). Anik F1 is generally brighter [26] than Anik G1, which permitted testing the cross-spectrum approach on a larger brightness difference of $\Delta m = 1.53$ magnitudes, corresponding to primary and secondary satellite magnitudes of 9.03 and 10.56 and a brightness ratio of $\alpha_b = 0.24$. This optical conjunction was predicted to not align as closely as the previous track pass; however, a short period during which the objects closed to within 3.4 arcseconds was observed. Figure 16 shows selected frames from the second optical conjunction.

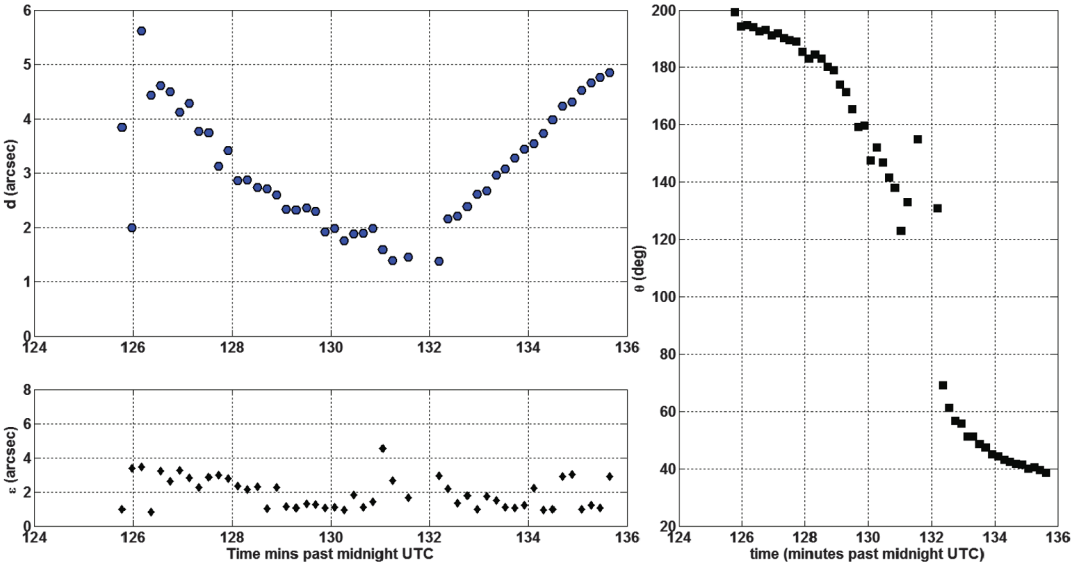


**Fig. 14 Optical conjunction of Anik G1 and Anik F1R on 18 February 2014. (Top left) Separation distance. (Right) Orientation angle $\theta$. (Bottom) Seeing $\varepsilon$.**

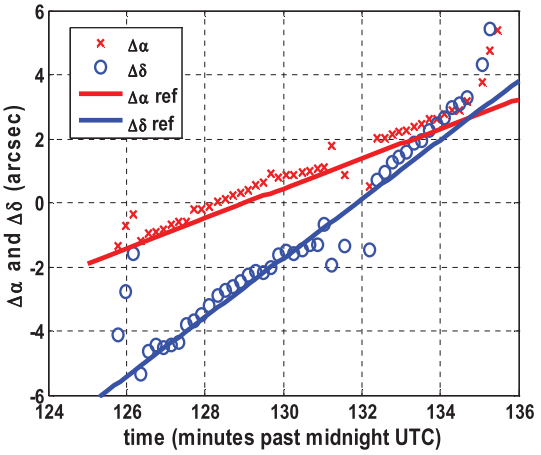


**Fig. 15 Anik G1 and Anik F1R $\Delta\alpha$ and $\Delta\delta$ measurements compared to reference ephemeris.**

A unique feature of this track was encountered at $t = 292$ min (see the third row of Fig. 16), where the seeing temporarily degraded to ~5 arcseconds for some of the speckle frames. Despite this seeing degradation, these high-seeing speckle measurements were processed, and the cross-spectrum measurements were found to be relatively insensitive this degradation. The degradation in the seeing was originally believed to be the cause of abnormal separation measurements (see Fig. 17) in which the separation measurements artificially swelled to ~4.5 arcseconds at $t = 292$ min. The algorithm that detects the first interior minima of the imaginary fringes was found to be ineffective at detecting the separation distance when high angular fringe rotation rates were encountered. The coincident seeing degradation was ultimately found to not be the root cause of the aberrant separation measurements. A more reliable technique for detecting the fringe minima at high angular fringe rotation rates was achieved by invoking a Fourier transform of the imaginary fringes and measuring distance between the spikes of high spatial power. By processing measurements in this manner, the track more closely adheres to the real relative motion between the objects (see the quadratic track of red squares in Fig. 17) and is much more tolerant to the fringe rotation effect during the satellites' closest approach.

Figure 18 shows $\Delta\alpha$ and $\Delta\delta$ measurements measured during this track using the separation measurements obtained via the Fourier transform of the imaginary fringes. Figure 18 shows good consistency with the measured differential angles measurements; however, a strong bias offset in differential right ascension was found, and Fig. 18 is bias corrected by −2.5 arcseconds to better show the second track's consistency with the reference ephemerides. The differential declination measurements did not exhibit a large bias and was not corrected. The 2.5 arcsecond discrepancy between the predicted and observed separations of the two satellites is suspected to be due to ranging system bias on Anik F1 placing Anik F1 nearly 0.5 km westward of Anik G1. The new fringe minima detection approach was not suspected to be the cause of the bias in differential right ascension. Some authors have indicated [27,28] that geostationary satellite ranging systems require regular bias correction as the bias manifests as an in-track position offset of satellite ephemerides in the inertial frame, which is consistent with the effect observed in $\Delta\alpha$. Without additional measurements, it is not possible to further analyze this behavior using a single track in order to further isolate the magnitude or its cause. Even with the new processing approach, approximately 0.5 arcseconds of deviation appears near $t = 292.5$ min, manifesting as a slight warp in positioning of the secondary; however, the effect is much less pronounced compared to the previous processing. The root-mean-square residuals from this track were better than the first and did not exceed 0.2 arcseconds, and areas outside of the slight warp at $t = 292.5$ min were better than 0.1 arcseconds.

## IX. Relative Orbit Estimates

Orbit estimation was performed on both tracks using an extended Kalman filter by applying the linearized measurement and dynamics model described in Secs. IV and V. Both tracks were initialized using the operator's orbital estimate with an initial position covariance for both objects set to $\boldsymbol{P} = \text{diag}[1^2, 1^2, 1^2, 0.001^2, 0.001^2, 0.001^2, 0.001^2]$ ($\text{km}^2, \text{km}^2/\text{s}^2, \text{m}^4/\text{kg}^2$) and process noise $\boldsymbol{Q}$ set to a $7 \times 7$ diagonal of small values of $(10^{-6})^2$.

The first track of Anik G1 and Anik F1R was initialized with a relative state vector with epoch 18 February 2014 2:05 UTC and state $\boldsymbol{x}_0 = [-9.936, 0.328, -0.038, 0.25e{-}3, 1.45e{-}3; 2.90e{-}3, 1.00e{-}3]^T$ $\times$(km,km/s,$\text{m}^2$/kg). Figure 19 shows that the relative position covariance exhibited a slight but noticeable growth of the radial position uncertainty ($\sigma_R$) despite additional differential angle measurements processed by the filter. The other two position states (in-track and cross-track) that largely correspond to the plane of sky measurements also exhibit growth, albeit to a lesser extent. As both in-track and radial directions are coupled in Hill's equations, the direct measurement of the secondary's in-track motion indirectly senses its radial component during estimation. The effect of convergence and observability of the radial motion due to this indirect sensing is discussed in Sec. X.

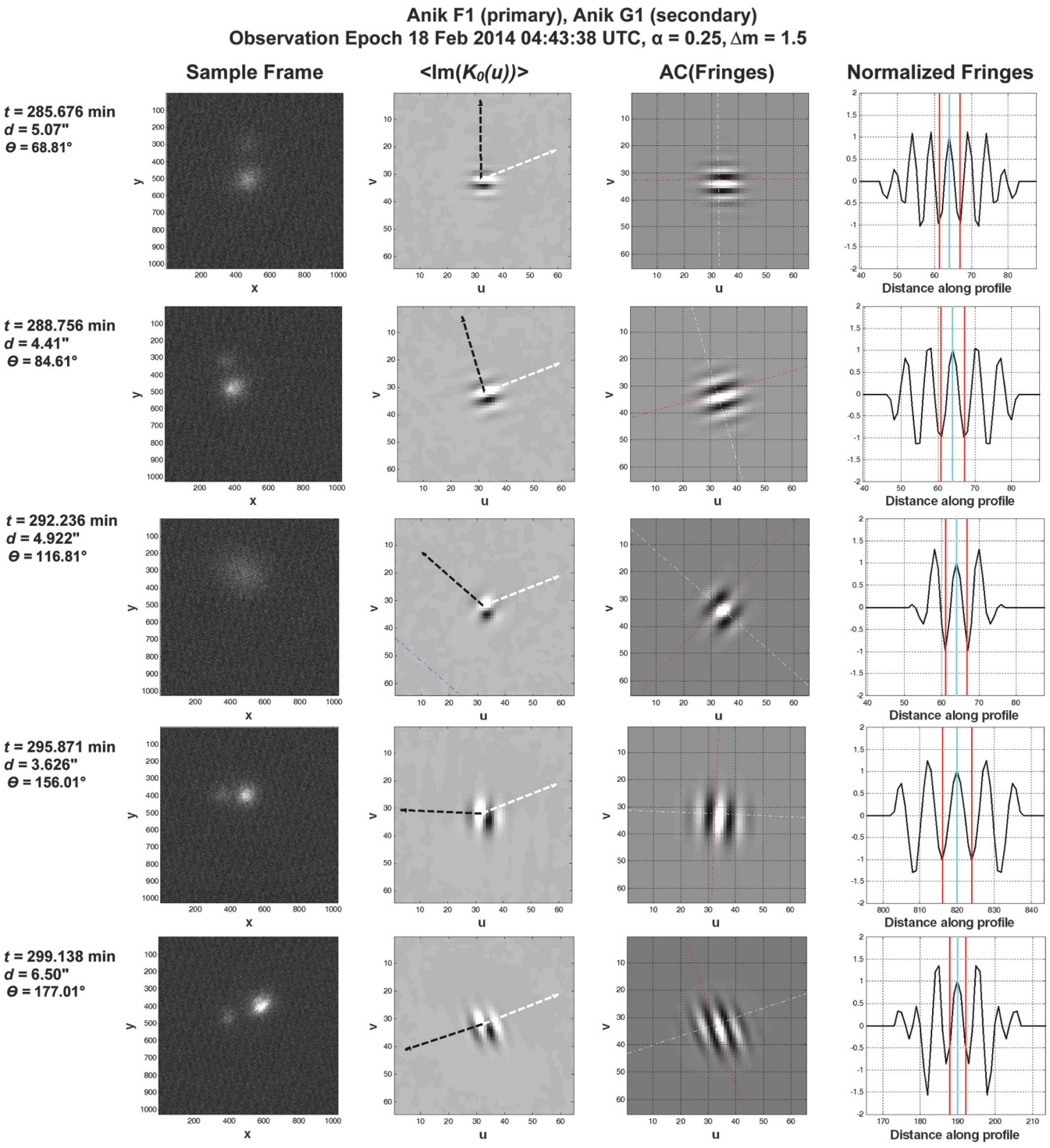


**Fig. 16 Anik F1 and Anik G1 selected frames from data processing for Anik F1 (primary) and Anik G1 (secondary) at the observation epoch on 18 February 2014, 04:43:38 UTC, $\alpha = 0.25$, $\Delta m = 1.5$.**

Figure 20 shows the estimated track of Anik G1 relative to Anik F1R. The track is smooth over the short tracking arc and adheres to the reference motion of the satellites well. Figure 21 shows the relative position error of the filtered position of Anik F1R in the radial, in-track, cross-track (RIC) frame with respect to its operator orbital ephemeris. Good consistency of the estimated relative orbit compared to the truth data was found with residuals not exceeding 100 m per axis. The spurious measurements caused by poorly formed fringes during the satellites' closest separation were properly rejected by the filter's 3-sigma rejection criteria.

The second track of Anik F1 and Anik G1 was initialized with a state vector with epoch 18 February 2014 at 4:43 UTC and initial relative position vector $\boldsymbol{x}_0 = [8.08, 1.56, -0.32, 0.02e-3, -1.22e-3, -1.72e-3, 1.00e-3]^T \times (\mathrm{km}, \mathrm{km/s}, \mathrm{m}^2/\mathrm{kg})$. Radial position error growth in this track closely mimicked the first track, reinforcing the need to inspect the attributes of the radial component convergence of the objects' motion. Anik G1's track relative to Anik F1 exhibited a noticeable in-track offset of ~500 m westward, reflecting the first observations accepted by the filter (see Fig. 22). This offset is attributed to the previously suggested ranging bias. Another feature of this track is a slight warp due to the radial position error being reestimated due to the in-track deviation initially encountered at the start of the track.

Figure 23 shows the consistency of Anik G1's position estimate relative to the operator ephemeris with respect to the RIC frame. The first measurements added to the filter caused an immediate −0.5 km westward (negative in-track) shift in Anik G1's position, reflecting

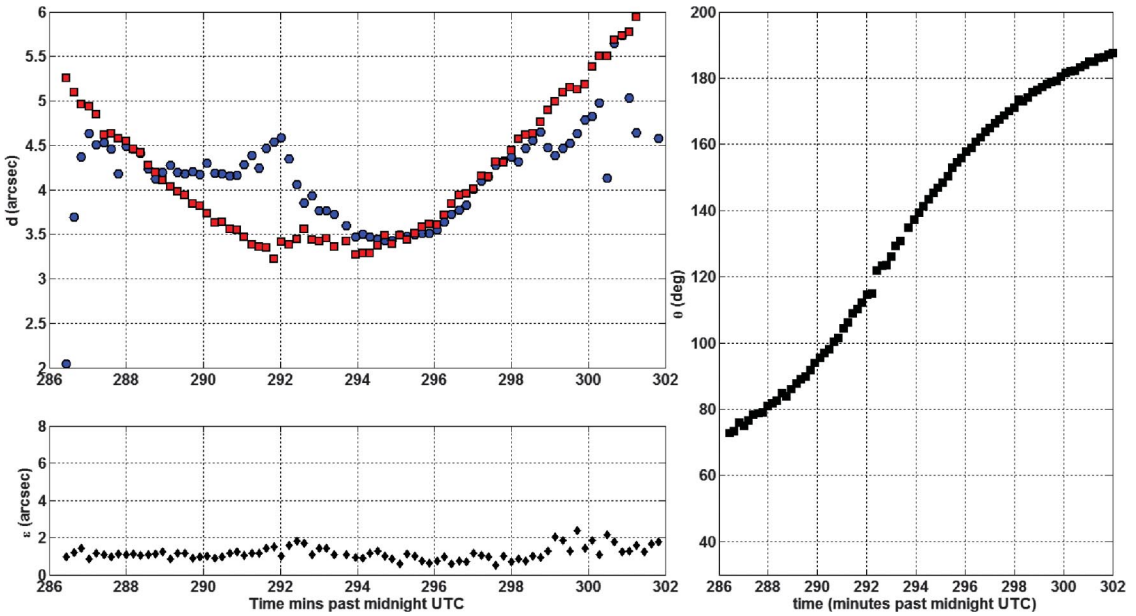


**Fig. 17 Optical conjunction of Anik F1 and Anik G1 on 18 February 2014. (Top left) Separation distance. (Right) Orientation angle $\theta$. (Bottom) Seeing $\varepsilon$.**

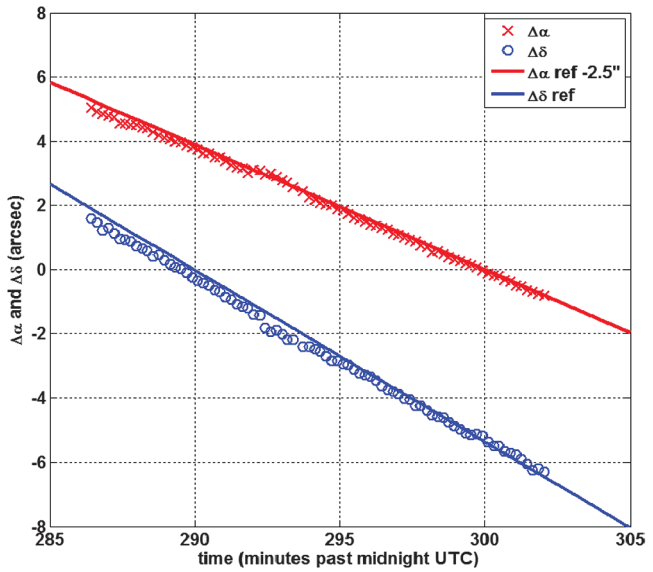


**Fig. 18 Anik F1 and Anik G1 $\Delta\alpha$ and $\Delta\delta$ measurements compared to reference ephemeris. $\Delta\alpha$ measurements are bias corrected by 2.5 arcseconds.**

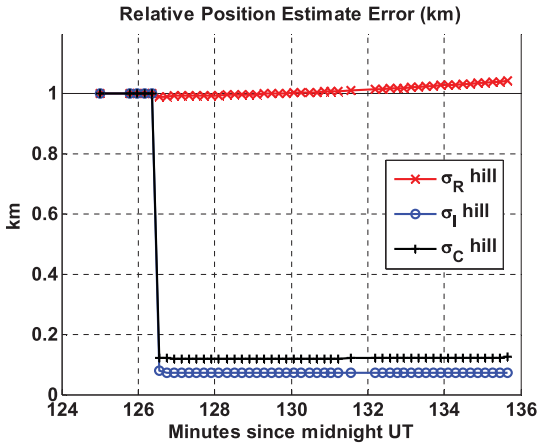


**Fig. 19 Anik G1 and Anik F1R relative orbit uncertainty.**

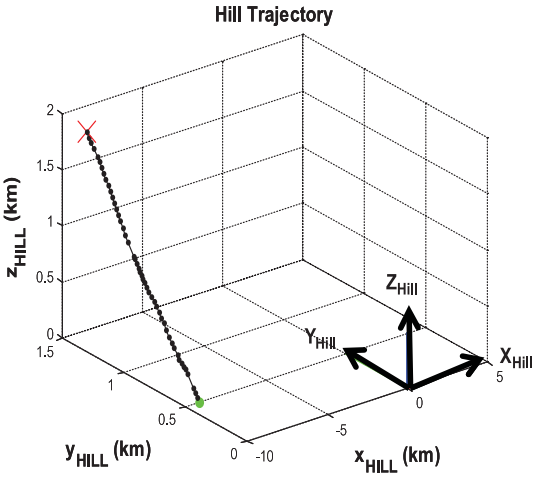


**Fig. 20 Anik G1 and Anik F1R relative trajectory. Green circle is track start, red x is track end.**

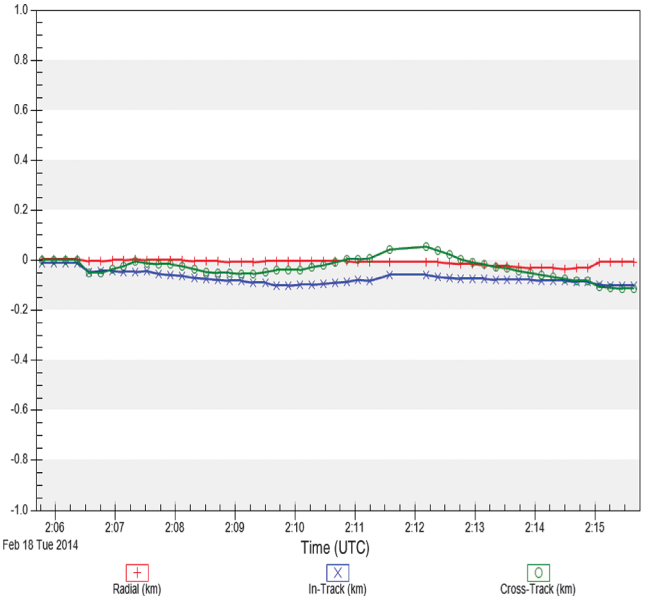


**Fig. 21 Anik G1 and Anik F1R RIC position error (km).**

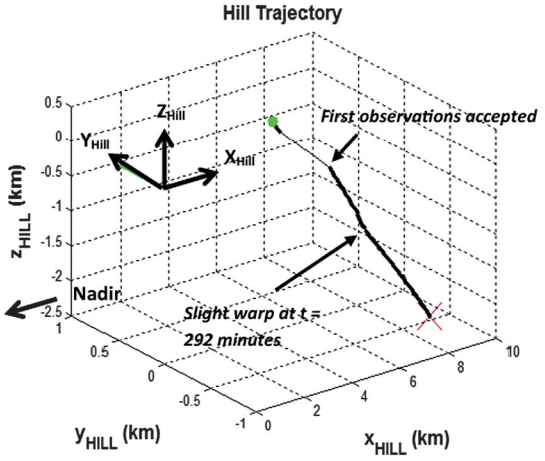


**Fig. 22 Anik F1 and Anik G1 relative trajectory.** Green = track **start.** Red = track **end.**

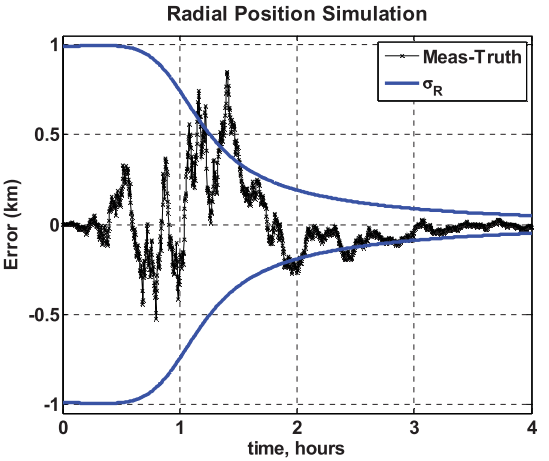


**Fig. 24 Simulated observations (measured truth) and radial position uncertainty ($\sigma_R$).**

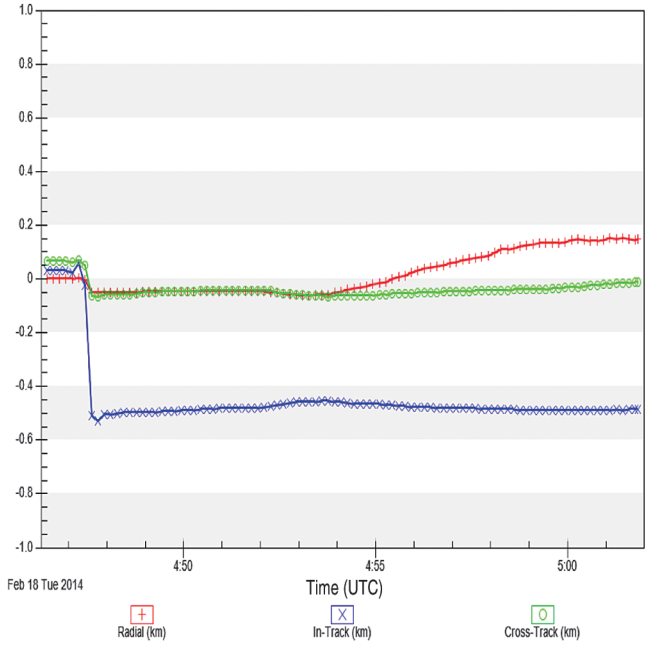


**Fig. 23 Anik F1 and Anik G1 RIC position error (km).**

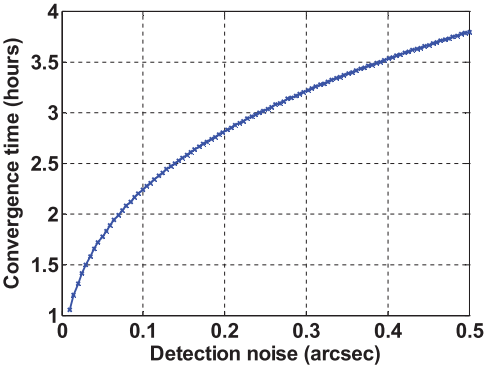


**Fig. 25 Convergence time vs measurement noise.**

the difference between the measured and predicted position of Anik G1 with respect to Anik F1. Observations were added to the filter until the time of high fringe rotation corresponding to the time of closest approach at $t = 292$ min (4:52 UTC in Fig. 23).

After closest approach, the radial position error grew, indicating that the filter was estimating a new radial position estimate. In contrast, the in-track and cross-track directions maintained relatively consistent error levels. The growth of the radial error is understandable given that the a priori state was not consistent with initial measurements. The filter attempted to resolve the radial component with the dynamically coupled in-track measurements, but a steady state was not achieved within the 15 min observation time frame as the radial position measurements continued to grow. The next section examines the behavior of filter convergence with respect to the radial component's behavior.

## X. Relative Orbit Convergence Analysis and Observability

The growth of the radial position uncertainty in Fig. 19 (and to a lesser extent the in-track and cross-track uncertainties) in both satellite tracks prompted an examination of the convergence of the filter. If the filter requires several days of observations to converge on a relative orbit estimate, the cross-spectrum differential angles technique would be of little practical value for space surveillance, especially for OOS monitoring. To examine the effect of the observational time span on filter convergence, a simulation using synthetic measurement data over longer data collection intervals (up to 12 h) was performed. This test indicated that the radial error grows for approximately 30 min and is followed by a steady convergence over a 3 h duration (see $\sigma_R$ in Fig. 24), regardless of the type of relative orbit. However, this positive result does not explain the reason for this behavior. The near colinearity of the observer's line of sight with the Hill frame's radial direction was suspected to impose an observability limitation as the radial component of the servicer's motion is indirectly sensed by measuring in-track motion from differential angle measurements and is examined in the next section.

An examination of the time required for the radial component of the covariance to converge to less than 10% of its initial value was performed by varying the sensor noise $\boldsymbol{R}_k = \text{diag}[\sigma^2_{\Delta\alpha}, \sigma^2_{\Delta\delta}]$. The filter's convergence was affected by the sensor noise precision mimicking a power law (see Fig. 25). Measurement noise from the Mont Mégantic experiment was ~0.25 arcseconds, so if it were possible to collect measurements on the satellite pair for 3 h, rather than the 15 minute period in which the two satellites met the isoplanatic condition, convergence of the relative orbit may have occurred.

Observation of a true OOS mission with a servicer perched close to the client is not likely to exhibit large relative motion, making longer observation periods viable. As telescopes are limited to night-time observing of ~12 h duration, these findings suggest that differential measurements for OOS relative orbit estimation are viable but that higher measurement precision is preferred. This favors larger aperture instruments and good PSF sampling in order to ensure highest precision measurements on the speckle imagery. The fringe rotating effect that was strongly observed in the second track is not

expected to be an issue for true, close-proximity OOS mission observations as the relative velocities between the objects are much lower than the collocated satellite cases observed from Mont Mégantic.

A test of observability can be performed by forming the matrix $\boldsymbol{Q}_0 = [\,\boldsymbol{H} \quad \boldsymbol{HA} \quad \cdots \quad \boldsymbol{HA}^{n-1}\,]^T$, where $\boldsymbol{A}$ is taken from Eq. (36) and $\boldsymbol{H}$ is taken from Eq. (46) and $n$ is the number of state variables. For the observation cases analyzed in this work, $\boldsymbol{Q}_0$ is full rank, indicating that the state is overall observable. Unfortunately, this insight does not lead to understanding the behavior of the transient convergence of the filter.

Observability expressed using the Jordan canonical form (JCF) [29] helps infer the relative degree of observability for each state variable. The JCF is found by forming

$$\boldsymbol{AV} = \boldsymbol{VJ} \tag{48}$$

where $\boldsymbol{V}$ is the linear transformation matrix that solves Eq. (48) and $\boldsymbol{J}$ is a diagonal matrix containing the solution's eigenvalues. The canonical form of the observation matrix is then

$$\bar{\boldsymbol{H}} = \boldsymbol{HV} \tag{49}$$

By inspecting the relative values in the columns in $\bar{\boldsymbol{H}}$, the sensitivity of the output measurements, as influenced by the changes in the state variables, can be compared [30]. Using the parameters for the observational geometry at Mont Mégantic, the canonical form of the observation matrix is

$$\bar{\boldsymbol{H}} = 1\times10^{-6}\begin{bmatrix} 0.011 & 6.887 & 75.382 & 75.382 & 0 & 0 \\ 0.0001 & 11.622 & 4.399 & 4.399 & 12.415 & 12.415 \end{bmatrix}$$

$\bar{\boldsymbol{H}}$ reveals that the first column consists of small numbers in comparison to the other columns, indicating that both measurements $\Delta\alpha$ and $\Delta\delta$ are only partially sensitive to the changes in the radial component $x_{\text{Hill}}$. While the relative orbit of the satellite pair is overall observable, the JCF analysis indicates that only partial observability exists for the radial component of the servicer's motion, pointing to the long time required for convergence to occur.

## XI. Conclusions

A cross-spectrum speckle interferometry approach adapted to monitor and track on-orbit servicing (OOS) formation flight in geostationary orbit was developed, and its limitations were explored. Experimental testing using collocated geostationary satellites with brightness differences of $m_{\text{primary}} = 10.2$, $\Delta m = 0.3$ and $m_{\text{primary}} = 9.1$, $\Delta m = 1.5$ achieved measurement precisions of 0.10–0.25 arcseconds, and relative orbits were estimated in both cases. The technique was shown to have three key limitations for OOS monitoring:

1) The observations must take place within the isoplanatic angle, which should not exceed 5 arcseconds.

2) The seeing should be much better than 4 arcseconds for the duration of the track.

3) Rhe seeing should be steady during measurement.

Relative orbits estimated using cross-spectrum speckle data produced tracks comparable to the orbital reference ephemeris provided by satellite operators; however, uncertainty of the radial positon grew during the 10 and 15 min tracking timeframes during both field tests. Separation measurement accuracy was affected at times of highest fringe rotation, and a technique to mitigate this effect was found.

Simulations show that relative orbit estimation requires approximately 3 h of tracking data to converge the radial position estimate, pointing to the need for longer observational arcs. Improvements in sensor noise can reduce filter convergence time, helping to increase the efficiency in an operational setting. An observability analysis shows that the motion of the servicer is overall observable; however, the radial component of the servicer's motion is shown to be only partially observable, pointing to the relatively long period of time required to converge an orbit estimate. This is attributed to the near-alignment of a ground-based camera's field of view with the in-track and cross-track directions of geostationary satellites.

The Mont Mégantic experimental observations provided valuable lessons on the use of speckle imaging for the observation of closely spaced satellites in geosynchronous equatiorial orbit. Speckle imaging can offer an economical approach for space surveillance tracking of OOS in geosynchronous orbit as a complimentary means to achieve space situational awareness of this new mission class.

## Appendix: Solar Radiation Pressure Perturbation

The solar radiation pressure acceleration is described by

$$\begin{bmatrix} a_x \\ a_y \\ a_z \end{bmatrix} = \begin{bmatrix} -\gamma P_{\text{sun}}\cos(\delta_{\text{sun}})\cos(\alpha-\alpha_{\text{sun}}) \\ -\gamma P_{\text{sun}}\cos(\delta_{\text{sun}})\sin(\alpha-\alpha_{\text{sun}}) \\ -\gamma P_{\text{sun}}\sin(\delta_{\text{sun}}) \end{bmatrix} \tag{A1}$$

where $\alpha_{\text{sun}}$ and $\delta_{\text{sun}}$ are the right ascension and declination of the sun and $\alpha$ is the right ascension of the satellite. The system of equations can be integrated by the use of

$$x(\alpha_1) = \Phi(\alpha_1-\alpha_0) + \gamma p(\alpha_1-\alpha_0) \tag{A2}$$

where the perturbation is expressed as

$$\gamma p(\alpha_1,\alpha_0) = \int_{\alpha_0}^{\alpha_1} \Phi_u(\alpha_1-\alpha) f(\alpha)\,\mathrm{d}\alpha \tag{A3}$$

where $f(s)$ is taken from Eq. (37) and $\Phi_u$ is taken from Eq. (38).

Performing the integration leads to the following set of equations that populates the augmented state transition matrix in Eq. (43):

$$p_1 = \frac{\gamma P_s\cos(\delta_{\text{sun}})}{4\omega}[5\cos(\alpha_{\text{sun}}-\alpha_1) - 8\cos(\alpha_{\text{sun}}-\alpha_0) + 3\cos(\alpha_{\text{sun}}-2\alpha_0+\alpha_1) - 2(\alpha_0-\alpha_1)\sin(\alpha_{\text{sun}}-\alpha_1)] \tag{A4}$$

$$p_2 = \frac{-\gamma P_s\cos(\delta_{\text{sun}})}{2\omega}[2\sin(\alpha_{\text{sun}}-\alpha_0) - 5\sin(\alpha_{\text{sun}}-\alpha_1) + 3\sin(\alpha_{\text{sun}}-2\alpha_0+\alpha_1) + 6(\alpha_0-\alpha_1)\cos(\alpha_{\text{sun}}-\alpha_0) + 2(\alpha_0-\alpha_1)\cos(\alpha_{\text{sun}}-\alpha_1)] \tag{A5}$$

$$p_3 = \frac{\gamma P_s\sin(\delta_{\text{sun}})}{\omega}[\cos(\alpha_0-\alpha_1)-1] \tag{A6}$$

$$p_4 = \frac{-\gamma P_s\cos(\delta_{\text{sun}})}{4}[3\sin(\alpha_{\text{sun}}-2\alpha_0+\alpha_1) - 3\sin(\alpha_{\text{sun}}-\alpha_1) + 2(\alpha_0-\alpha_1)\cos(\alpha_1-\alpha_{\text{sun}})] \tag{A7}$$

$$p_5 = \frac{-\gamma P_s\cos(\delta_{\text{sun}})}{2}[3\cos(\alpha_{\text{sun}}-\alpha_1) - 6\cos(\alpha_{\text{sun}}-\alpha_0) + 3\cos(\alpha_{\text{sun}}-2\alpha_0+\alpha_1) - 2(\alpha_1-\alpha_0)\sin(\alpha_1-\alpha_{\text{sun}})] \tag{A8}$$

$$p_6 = \gamma P_s\sin^2(\delta_{\text{sun}})[\sin(\alpha_1-\alpha_0)] \tag{A9}$$

## Acknowledgments

This work was supported by Defence R&D Canada's Ottawa Research Center's 05BA Space Situational Awareness project. The authors wish to acknowledge the Department of National Defence;

the Department of Mechanical and Aerospace Engineering at Carleton University; Telesat Canada; University of Montreal; Observatoire du Mont-Mégantic; and Nuvu Camera, Inc., for their support of this work.

## References

[1] Orloff, R. W., "Space Shuttle Mission STS-41C Press Kit," NASA Release No. 84-38, March 1984, http://www.jsc.nasa.gov/history/shuttle_pk/pk/Flight_011_STS-41C_Press_Kit.pdf [retrieved 28 Aug. 2014].

[2] "STS-88 ISS Construction Mission," NASA, http://science.ksc.nasa.gov/shuttle/missions/sts-88/mission-sts-88.html [retrieved 10 Jan. 2010].

[3] Madison, R., "Micro-Satellite Based, On-Orbit Servicing Work at the Air Force Research Laboratory," *IEEE Aerospace Conference*, Inst. of Electrical and Electronics Engineers, Piscataway, NJ, 2000, pp. 215–226.

[4] "Robotic Refueling Mission, NASA Facts, Satellite Servicing Capabilities Office," NASA, http://ssco.gsfc.nasa.gov/images/RRM_2013_Factsheet_07.pdf [retrieved 15 May 2015].

[5] Mulder, T., "Orbital Express Autonomous Rendezvous and Capture Flight Operations, Part 1 of 2: Mission Description, AR&C Exercises 1, 2, 3," *Spaceflight Mechanics Meeting*, American Astronautical Soc. Paper 08-209, Univelt, San Diego, CA, 2008.

[6] Labeyrie, A., "Attainment of Diffraction Limited Resolution in Large Telescopes by Fourier Analyzing Speckle Patterns in Star Images," *Astronomy and Astrophysics*, Vol. 6, 1970, pp. 85–87.

[7] Worden, S., "Speckle Interferometry I: A Test on an Earth Orbital Satellite," Air Force Geophysics Lab., Hanscom Air Force Base Technical Rept. AFGL-TR-82-0340, Bedford, MA, Nov. 1982.

[8] Lawrence, T. W., Goodman, D. M., Johansson, E. M., and Fitch, J. P., "Speckle Imaging of Satellites at the U.S. Air Force Maui Optical Station," *Applied Optics*, Vol. 31, No. 29, 1992, pp. 6307–6321. doi:10.1364/AO.31.006307

[9] Fried, D. L., "Optical Resolution Through a Randomly Inhomogeneous Medium for Very Long and Very Short Exposures," *Journal of the Optical Society of America*, Vol. 56, No. 10, Oct. 1966, pp. 1372–1379. doi:10.1364/JOSA.56.001372

[10] Beavers, W. I., Dudgeon, D. E., Beletic, J. W., and Lane, M. T., "Speckle Imaging Through the Atmosphere," *Lincoln Laboratory Journal*, Vol. 2, No. 2, Nov. 1989, pp. 207–228.

[11] Roddier, F., Gilli, J. M., and Vernin, J., "On the Isoplanatic Patch Size in Stellar Speckle Interferometry," *Journal of Optics*, Vol. 13, No. 2, 1982, pp. 63–70.

[12] Bagnuolo, W. G., Mason, B., and Barry, D. J., "Absolute Quadrant Determinations from Speckle Observations of Binary Stars," *Astronomical Journal*, Vol. 103, No. 4, 1992, pp. 1399–1407. doi:10.1086/116155

[13] Aristidi, E., Carbillet, M., Lyon, J.-F., and Aime, C., "Imaging Binary Stars by the Cross-Correlation Technique," *Astronomy and Astrophysics Supplement Series*, Vol. 125, No. 1, 1997, pp. 139–148. doi:10.1051/aas:1997215

[14] Knox, K., "Measuring Close Binary Stars with Speckle Interferometry," *Proceedings of the AMOS Technical Conference*, Maui Economic Development Board, Kihei, HI, 2014.

[15] Scott, R. L., and Ellery, E., "An Approach to Ground Based Space Surveillance of Geostationary On-Orbit Servicing Operations," *Acta Astronautica*, Vol. 112, July–Aug. 2015, pp. 56–68. doi:10.1016/j.actaastro.2015.03.010

[16] Vallado, D. A., *Fundamentals of Astrodynamics and Applications*, 4th ed., Microcosm, Hawthorne, CA, 2013, pp. 389, 207, 396.

[17] Vallado, D. A., and Alfano, S., "Curvilinear Coordinates for Covariance and Relation Motion Operations," *Astrodynamics Specialist Conference*, American Astronautical Soc. Paper 11-464, Girdwood, AK, July 2011.

[18] Clohessy, W. H., and Wiltshire, R. S., "Terminal Guidance System for Satellite Rendezvous," *Journal of Aerospace Sciences*, Vol. 27, No. 9, 1960, pp. 653–658, 674. doi:10.2514/8.8704

[19] Hill, G., "Researches in Lunar Theory," *American Journal of Mathematics*, Vol. 1, No. 1, 1878, pp. 5–26. doi:10.2307/2369430

[20] Kawase, S., "Real Time Relative Motion Monitoring for Co-Located Geostationary Satellites," *Journal of the Communications Research Laboratory*, Vol. 36, No. 148, 1989, pp. 125–135.

[21] Mason, B., "Atmospheric Dispersion and Risley Prisms," U.S. Naval Observatory, Double Star Rept. No. 3, Jan. 2003.

[22] Scott, R. L., and Wallace, B. J., "Small Aperture Telescope Observations of Co-Located Geostationary Satellites," *Proceedings of the AMOS Technical Conference*, Maui Economic Development Board, Kihei, HI, 2009.

[23] Drissen, L., Bastien, P., Lafreniere, R., Doyon, R., Thibault, S., Hernandez, O., and Lamontange, R., "Innovation in Astronomical Instruments at the Observatoire du Mont-Megantic," *Physics in Canada*, Vol. 71, No. 1, Jan. 2015, pp. 24–26.

[24] Daigle, O., Gach, J., Guillaume, C., Lessard, S., Carignan, C., and Blais-Ouellette, S., "CCCP: A CCD Controller for Counting Photons," *Proceedings of SPIE 7014, Ground-Based and Airborne Instrumentation for Astronomy II*, July 2008, Paper 70146L.

[25] Moffat, A. F. J., "A Theoretical Investigation of Focal Stellar Images in the Photographic Emulsion and Application to Photographic Photometry," *Astronomy and Astrophysics*, Vol. 3, 1969, pp. 455–461.

[26] Scott, R., and Wallace, B., "Small-Aperture Optical Photometry of Canadian Geostationary Satellites," *Canadian Aeronautics and Space Journal*, Vol. 55, No. 2, 2009, pp. 55–67. doi:10.5589/q09-004

[27] Oltrogge, D., and Alfano, S., "COMSPOC Update and Operational Benefits," *31st Space Symposium*, The Space Foundation, Colorado Springs, CO, 2015.

[28] Sawada, F., and Kawase, S., "Relative Orbit Determination Experiment by Ground-Based Differential Angle Tracking," *Electronics and Communications in Japan*, Vol. 79, No. 1, 1996, pp. 97–106. doi:10.1002/ecja.4410790110

[29] Crassidis, J. L., and Junkins, J. L., *Optimal Estimation of Dynamic Systems*, CRC Press, Boca Raton, FL, 2004, pp. 585–587.

[30] Levesque, J. F., and De Lafontaine, J., "Innovative Navigation Schemes for State and Parameter Estimation During Mars Entry," *Journal of Guidance, Control, and Dynamics*, Vol. 30, No. 1, 2007, pp. 169–184. doi:10.2514/1.25107

A. V. Rao
*Associate Editor*